Active *Q* Flux Concept for Sensorless Control of Synchronous Reluctance Machines

Zhendong Zhang , *Member, IEEE*, and Jacob Lamb , *Member, IEEE*

Abstract—In this article, we propose a new scheme to use active flux on the *q*-axis for sensorless control of synchronous reluctance machines (SynRMs). Conventionally, "active flux" on the *d*-axis is adopted to convert a salient-pole machine into a fictitious nonsalient-pole machine. However, the injected *d*-axis flux can deteriorate high-frequency injection (HFI) sensorless control performance or even run the system into unstable region at low speed. This article demonstrates that active flux on the *q*-axis can support back EMF sensorless control at high speed and improve low-speed HFI performance substantially. A seamless transition from HFI sensorless method to back EMF voltage method is attained after adopting the proposed active *q* flux. The experimental results are used to validate the proposed method.

Index Terms—Active flux, back electromotive force (EMF), high-frequency injection (HFI), saliency, sensorless control, synchronous reluctance machines (SynRMs).

I. INTRODUCTION

SYNCHRONOUS reluctance machines (SynRMs) exhibit higher efficiency and better torque density as compared to induction machines (IM) [1], and better cost reduction, less resource security risk, and higher reliability as compared to permanent-magnet (PM) machines [2]. Thanks to these advantages, SynRMs are becoming more popular, especially for industrial application where sizing is not a deterministic factor. Since both SynRM and IM do not use expensive rare-earth materials, replacing the existing IM with more efficient SynRM is demonstrated to be a feasible and rewarding solution.

SynRM are one type of salient-pole machine that have structural similarities toward widely used interior permanent-magnet (IPM) machines. However, SynRM control is distinct from IPM machine control, mainly due to the self-saturation and cross-saturation between *d* and *q* axes and the lack of rotor PMs.

Sensorless control of SynRM has been investigated by a number of authors, and the hybrid high-frequency injection (HFI)

and back electromotive force (EMF) sensorless methods are widely adopted [3]–[12]. The same sensorless control methods that apply to IPM machines, whether it is HFI method or back EMF method, can be deployed to SynRM potentially. However, self-saturation and cross-saturation of SynRM could complicate the implementation. In particular, the HFI sensorless method, which relies on machine saturation level, requires re-evaluation and recommissioning. A reference *q*-axis current, saturating *q*-axis iron, is reported to improve HFI sensorless performance at low speed [5], [13], [14].

However, all these reference methods require a minimum magnetizing current (*d*-axis current) to flux-up the machine for the purpose of providing "active flux" for angle detection. The active flux concept [15], assisting the back EMF-based sensorless control for a salient-pole machine, is proposed and, therefore, rotor position can be retrieved directly just as a nonsalient-pole machine. Despite rotor position is only detected by HFI method at low speed, this active flux is still maintained for the purpose of a seamless transition from HFI scheme to back EMF scheme and vice-versa. However, injecting *d*-axis current can reduce motor saliency substantially or even reverse motor saliency, which could deteriorate HFI sensorless performance since the angle detection accuracy of HFI method heavily relies on machine saliency.

Instead of doing sensorless control using the *d*-axis current-induced active flux above, this article proposes a new approach that uses the *q*-axis current-induced flux for SynRM back EMF-based sensorless control. Conceptually, *q*-axis current is considered as torque current, which should not be used for flux excitation and sensorless control. However, it is verified by experimental results that the *q*-axis current-induced flux offers not only sensorless capability but also benefits compared to the *d*-axis current. This new *q*-axis current-induced flux is defined as "active *q* flux" throughout this article. Although the proposed active *q* flux does not change any existing HFI algorithms, it indirectly helps the HFI performance at low speed [5], [16].

The rest of this article is organized as follows. Section II reviews the background knowledge about SynRM. Section III evaluates the conventional scheme of doing SynRM sensorless control. The active *q* flux concept is proposed in Section IV and sensorless control using active *q* flux concept is presented. In Section V, the experimental data validate that the proposed active *q* flux concept can improve HFI angle detection stability while maintain sensorless performance based on the back EMF method. Finally, Section VI concludes this article.
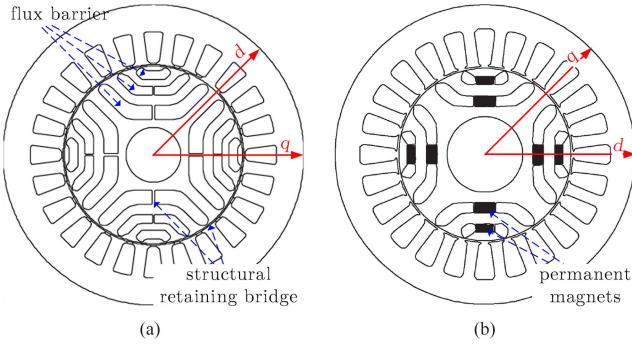
Fig. 1. SynRM and IPM motor stator and rotor cross-sectional lamination [35].

Fig. 2. 3-kW SynRM current-to-flux-linkage map evaluated from experiments.

II. SynRM Background

In this section, the rotor structures of both SynRM and IPM machine are compared, and SynRM mathematical model is reviewed. Additionally, the flux vector control (FOC) of SynRM below base speed using maximum torque per ampere (MTPA) scheme is briefly described.

A. SynRM and IPM machine Rotor Structure Comparison

Unlike IPM machines with magnets on the rotor, the rotor of SynRM is made of steel lamination only, either in transverse direction or in axial direction. Fig. 1(a) shows the cross-sectional view of the stator and rotor laminations of a typical four-pole SynRM. Its stator is very similar to IM and PM machines. A few layers of flux barrier create high reluctance radial path. Normally, the d-axis is defined toward the high permeance path (iron dominant), while the q-axis aligns to the low permeance path (air dominant). Fig. 1(b) shows the cross section of an IPM machine, which possesses a similar stator and rotor structure as compared to that in Fig. 1(a), except for the highlighted PMs. Note, in particular, that the definition of d and q axes for an IPM machine in Fig. 1(b) is different from that for a SynRM in Fig. 1(a). The d-axis of an IPM machine is defined along low permeance path and the q-axis is defined along high permeance path.

B. SynRM Mathematical Model

SynRM mathematical model in the dq axes rotor reference frame is specified as follows:

$$\begin{cases} v_d = R_s\,i_d + \frac{d\lambda_d}{dt} - \omega\lambda_q \\ v_q = R_s\,i_q + \frac{d\lambda_q}{dt} + \omega\lambda_d \end{cases} \tag{1}$$

$$\begin{cases} \lambda_d = \lambda_d\,(i_d, i_q) = L_{dd}i_d + L_{dq}i_q = L_d\,(i_d, i_q)\cdot i_d \\ \lambda_q = \lambda_q\,(i_d, i_q) = L_{qd}\,i_d + L_{qq}\,i_q = L_q\,(i_d, i_q)\cdot i_q \end{cases} \tag{2}$$

$$T = \frac{3}{2}\,p\,(\lambda_d i_q - \lambda_q i_d) \tag{3}$$

where R_s is the stator resistance, ω is the rotor frequency, p is the pole pairs, v_d and v_q are the stator dq voltages, i_d and i_q are the stator dq currents, λ_d and λ_q are the stator dq voltages, and T denotes the electromagnetic torque. In (2), L_{dd} and L_{qq}

are the dq axes self-inductance. L_{dq} is the d-axis cross-saturation inductance induced from the q-axis current, and L_{qd} is the q-axis cross-saturation inductance induced from the d-axis current. Both dq axes self-inductance and cross-saturation inductance can be lumped together as $L_d(i_d, i_q)$ and $L_q(i_d, i_q)$ in (2). Equation (2) can be expressed using two two-dimensional (2-D) flux maps with i_d, i_q as the index axes, namely current-to-flux-linkage map. Fig. 2 shows the flux map of the SynRM under test and its full specification is shown in Table I. The flux map defines the basic characteristic of this SynRM and provides data necessary for control. Fig. 2 is identified through the offline dyne test, although it can also be evaluated through finite-element analysis or online self-commissioning method [17], [18].

C. FOC Vector Control Scheme

The FOC scheme of a SynRM is shown in Fig. 3. FOC can be implemented with position sensor or without position sensor. If sensorless control is preferred, a position and speed observer is needed to estimate the rotor position information out of machine voltages and currents. For flux and torque control, the conventional dq dual axes current regulators are one of the solutions. A flux regulator, replacing the d-axis regulator, is reported in [19], considering the d-axis as the flux axis and q-axis as the torque axis. A d-axis flux estimator is then needed to assist the implementation of this method.

Low-speed MTPA control and high-speed flux weakening control are established control strategy for salient-pole machines. These optimal current control trajectories on $i_d - i_q$ vector plane can be obtained based on the map in Fig. 2. The detailed analysis and commissioning of MTPA curve can be found in the existing published pieces of literature [20], [21]. This article focuses on sensorless control and MTPA operation

TABLE I
SynRM Specifications

SynRM motor under test	
Rated Power	3.0 kW
Rated Speed	1500 rpm
Rated Torque	19 N·m
Nominal Line-Line Voltage (rms)	380 V
Nominal Current (rms)	7.1 Arms
Switching Frequency	4 kHz
Number of poles	4 poles
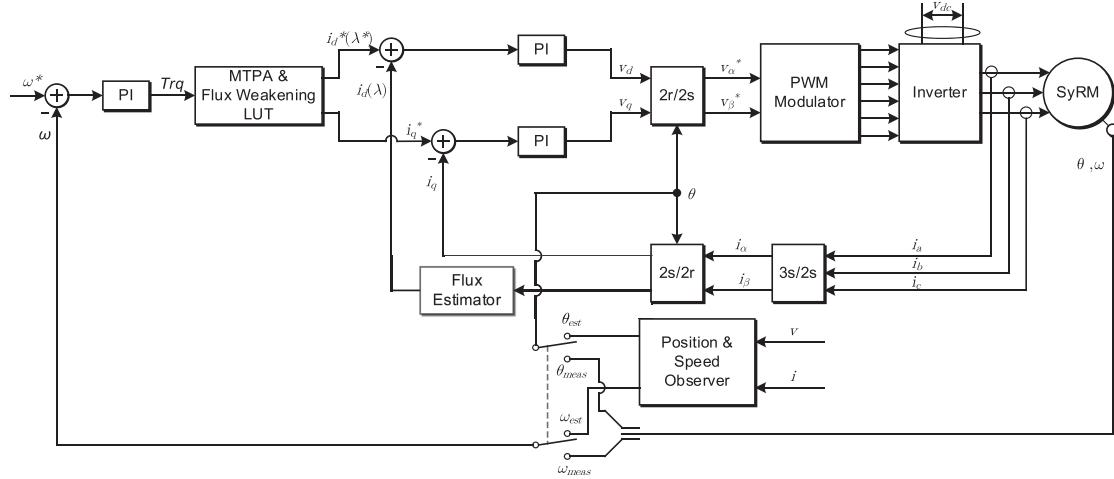
Fig. 3.   SynRM FOC control block diagram.
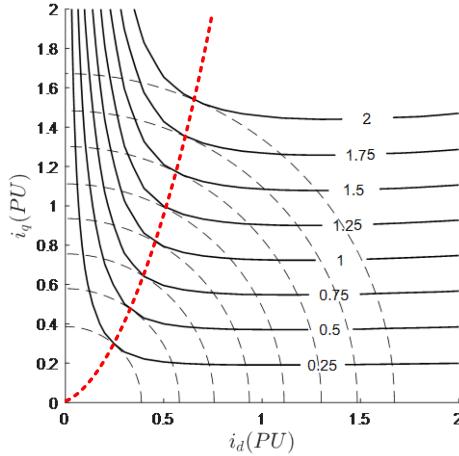
Fig. 4.   3-kW SynRM constant torque curve and MTPA curve. Red dotted line is the MTPA trajectory, solid lines are the torque contours, and dashed lines are the current—magnitude contours.

below base speed. The constant torque curve and MTPA curve of the SynRM under test are plotted in Fig. 4.

III. SYNRM SENSORLESS CONTROL

As mentioned earlier, sensorless algorithms that apply to IPM machines need re-evaluation and potential adjustments to ensure reliable operation for SynRM. This section first reviews the existing sensorless control methods for SynRM. The unique challenges of controlling a SynRM is explained, and the limitations of existing methods are explored.

A. Low-Speed High-Frequency Injection

For a salient-pole machine, HFI can be used to extract rotor position at low speed [22], [23]. All HFI methods that apply to IPM machines, whether it is sinusoidal waveform injection [24], or the pulsating voltage injection [25], [26], or the square waveform injection [27], should be viable for SynRM. However,
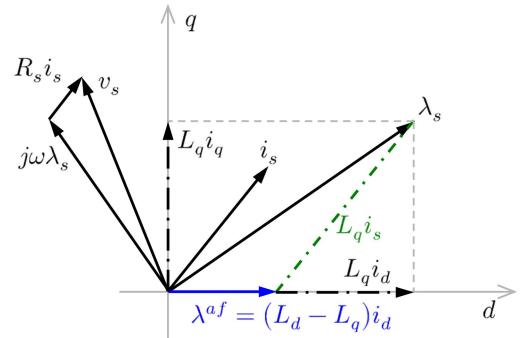
Fig. 5.   Active flux definition in the *dq* axes frame.

dq axes self-saturation and cross-saturation does affect angle detection substantially [28] and will be studied in-depth below.

Since the proposed active *q*-axis flux concept is intended for operation at higher speeds, any complementary HFI method for low-speed operation is necessary for acceptable performance. The detailed selection of HFI method is independent of implementing the proposed method and will not be expanded in this article.

B. Combined Active Flux Concept and HFI Methods

HFI method is normally applied at low speed to prevent aliasing between the fundamental component and high-frequency component. Back EMF voltage-based sensorless takes over after the motor accelerates over certain threshold speed. "Active flux" model [15] is normally employed to turn an anisotropic machine into a fictious isotropic machine. It is expressed as

$$\begin{cases} \lambda_d^{af} = \lambda_d - L_q\,i_d = (L_d - L_q)\,i_d = \lambda^{af} \\ \lambda_q^{af} = \lambda_q - L_q\,i_q = 0 \end{cases} \tag{4}$$

where λ^{af} is the active flux, and λ_d^{af} and λ_q^{af} are the active fluxes on the *dq* axes. As illustrated in Fig. 5, active flux is derived graphically on *dq* axes vector plane based upon (4), where $L_q i_s$ vector in green dot-dash line is to derive active
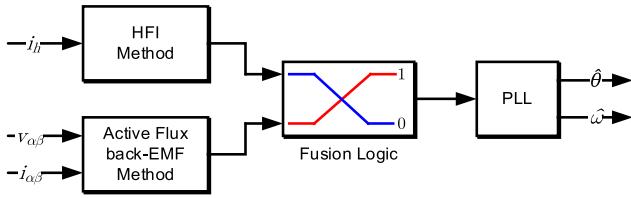
Fig. 6. Estimated angle fusion from HFI method and active flux method.

flux λ^{af} from stator flux λ_s. Thus, the voltage equation in α, β stationary reference frame can be retrieved by substituting (4) into (1) and transforming the dq axes into α, β axes using rotor angle θ as follows:

$$\begin{bmatrix} v_\alpha \\ v_\beta \end{bmatrix} = \left(R_s + \frac{d}{dt} L_q \right) \begin{bmatrix} i_\alpha \\ i_\beta \end{bmatrix} + \omega \lambda^{af} \begin{bmatrix} -\sin\theta \\ \cos\theta \end{bmatrix}. \quad (5)$$

Torque equation can also be derived as follows:

$$T = \frac{3}{2} p \left[(L_d - L_q) i_d i_q \right] \quad (6)$$

$$T = \frac{3}{2} p \lambda^{af} i_q \quad (7)$$

where v_α and v_β are the stator $\alpha\beta$ voltage, i_α and i_β are the stator $\alpha\beta$ current, and θ is the rotor electrical angle. Simply applying integration toward the voltage model in (5), (8)–(10) show how to calculate rotor position using the active flux concept

$$\begin{cases} \lambda_{s\alpha} = \int (v_\alpha - R_s i_\alpha)\, dt \\ \lambda_{s\beta} = \int (v_\beta - R_s i_\beta)\, dt \end{cases} \quad (8)$$

$$\begin{cases} \lambda_\alpha^{af} = \lambda_{s\alpha} - L_q i_\alpha \\ \lambda_\beta^{af} = \lambda_{s\beta} - L_q i_\beta \end{cases} \quad (9)$$

$$\theta = \operatorname{atan} \left(\frac{\lambda_\alpha^{af}}{\lambda_\beta^{af}} \right) \quad (10)$$

where $\lambda_{s\alpha}$ and $\lambda_{s\beta}$ are the stator $\alpha\beta$ flux linkage. λ_α^{af} and λ_β^{af} are the active fluxes on the $\alpha\beta$ axes. These equations explain the basic mathematics for rotor position estimation, while more advanced schemes, such as observer-based estimation algorithms, can be deployed.

A fusion logic, as shown in Fig. 6, is then adopted to do a smooth transition between HFI scheme at low-speed and back EMF scheme at high speed when motor accelerates or decelerates.

C. MTPA and Minimum Excitation Current Selection

The MTPA curve in Fig. 4 shows the operating trajectory with highest torque output while having lowest current magnitude. When near zero torque is commanded, both i_d and i_q command currents are close to the origin based on MTPA curve. Sensorless operation of SynRM becomes challenging at this region mainly due to two reasons.

1) When i_d is close to zero, the active flux vector, as depicted in Fig. 5 and (4), is also adjacent to zero, and therefore, back EMF sensorless control that requires enough active
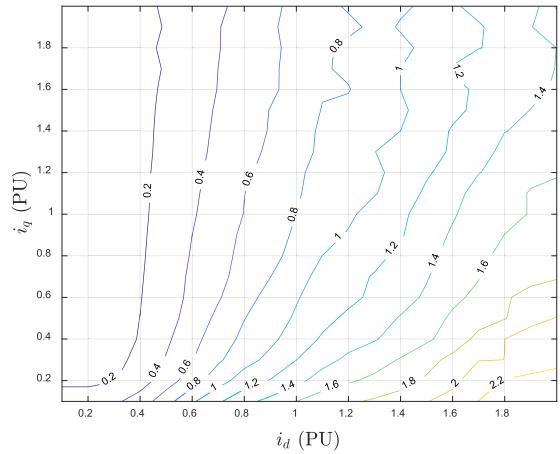
Fig. 7. Saliency ratio on i_d–i_q current vector plane based on the transient inductance. Note that the saliency ratio contours shown in the figure may deviate away from the actual saliency ratio of the machine when $|i| \approx 0$ primarily due to testing granularity and measurement.

flux may not offer reliable angle detection under this circumstance.

2) When i_d and i_q are both around zero, neither the d-axis nor q-axis flux paths in Fig. 1(a) are saturated [5]. In this case, the transient inductance between d and q axes could stay close, which indicates a near unity saliency ratio (L_q/L_d). However, HFI method requires a minimum saliency ratio for reliable rotor position detection. This will be further expanded below.

To overcome issue 1), a minimum i_d current is preselected to guarantee enough active flux for back EMF-based sensorless angle detection [4], [7]. It may also improve sensorless performance caused by issue 2). However, it could run into the risk of entering unstable region when HFI is enabled, which is dependent on machine design characteristics. Although a saturation i_q current is proposed in [5] to resolve issue 2), a 2-D hysteresis transition scheme is needed to transit from saturation i_q current at low speed to minimum i_d current at high speed, which can complicate system design and introduce extra disturbance into the system.

D. Absence of Saliency and Reverse Saliency

For each d-axis flux λ_d in Fig. 2, it has a knee point ($i_d \approx 4$ A), where transient inductance is markedly different before and after the knee point. This is attributed to the fact that the d-axis lamination steel starts to saturate when excessive i_d current is injected. In other words, SynRM gradually lose saliency when more i_d current is injected. Fig. 7 shows saliency ratio on dq axes current plane, which is derived from the flux map in Fig. 2.

Normally, SynRM HFI angle detection is based on the assumption that $L_d \gg L_q$. However, this is not always valid on the whole current vector plane. The case when $L_d \approx L_q$ is mentioned in Section III-C above. For extreme condition, where large i_d and small i_q are injected, the case where $L_d < L_q$ can occur, which is named "reverse saliency." Some methods may
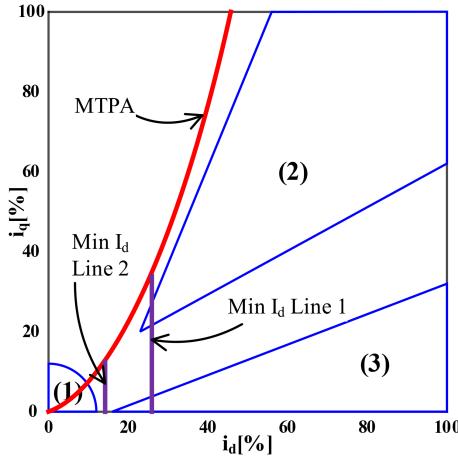
Fig. 8. SynRM HFI unstable regions.

be able to continue working in this region [29], while other algorithms will result in a 90° phase shift.

Both "absence of saliency" and "reverse saliency" will lead to the failure of reliable and consistent angle detection for any HFI scheme in these regions.

E. Stability Region for HFI Sensorless Angle Detection

Section III-C and D above address stability issue regarding back EMF and HFI schemes for SynRM sensorless control. The minimum i_d excitation resolves back EMF scheme issue, while the stability issue regarding HFI operation remains. In this section, three HFI instability regions are highlighted in Fig. 8 with each region explained below to assist the development of new solution.

Region (1): Neither d nor q axes are saturated.

Issue 2) in Section III-C is referring to the same instability region, which is known as rib effect [30]. The q-axis needs structural retaining ribs between each flux barrier layer to enhance the structural strength of the rotor lamination, as shown in Fig. 1(a). These tiny ribs create a low magnetic resistance path along the q-axis. These ribs will soon become saturated when very little i_q current is injected, which certainly helps create rotor saliency. Otherwise, the rotor will not show enough saliency for reliable HFI angle detection when the current vector falls inside zone (1), as shown in Fig. 8.

Region (2): d and q axes are both saturated.

Large torque requires large i_d and i_q currents output. According to the flux curve in Fig. 2, both d and q axes run into flux saturation in this case. Defining a boundary for Region (2) based on the saliency data is difficult because HFI methods will typically begin to fail at saliency ratios below unity. The actual saliency value where a given HFI method begins to fail is dependent upon numerous factors. In general, it is good practice to ensure a wide margin between an operating point and regions of instability.

Region (3): d-axis is saturated, but q-axis is not.

HFI works well assuming $L_d \gg L_q$. When large d-axis current is injected while no q-axis current is injected, the reverse

relationship $L_d < L_q$ holds. In this case, HFI detected angle has 90° tracking error.

To avoid all HFI instability regions, the selection of minimum d-axis current curve becomes challenging. Fig. 8 shows two min i_d lines (Min I_d Line 1 and Min I_d Line 2) with different i_d value. Min I_d Line 1 falls inside unstable regions (2) and (3), while Min I_d Line 2 does not. Identifying stable min I_d line requires exact knowledge of the plant, which may not be readily available. It is possible that no minimum d-axis trajectory can avoid all three regions considering unique machine designs.

Fig. 8 shows that the region to the left of MTPA curve (excluding Region 1) never falls inside any of these HFI unstable regions mentioned above. However, this operation region cannot satisfy the minimum d-axis excitation trajectory, which is required by back EMF active flux angle detection. One potential solution is to transit from minimum q-axis current trajectory to minimum d-axis trajectory instantaneously during HFI method and back EMF method fusion period, as shown in Fig. 6. However, this could result in large disturbance, or even worse, transition failure.

IV. PROPOSED ACTIVE Q FLUX CONCEPT FOR SYNRM SENSORLESS OPERATION

Section III reviews sensorless control of a SynRM and stability challenge associated especially for HFI. In this section, a new solution is proposed to address the dilemma that the current trajectories for HFI stable operation and that for back EMF operation do not align with each other. By adopting the proposed solution, sensorless control performance of a SynRM can be substantially improved.

An IPM machine uses rotor PM-induced d-axis flux for back EMF sensorless control. Since d and q axes are flipped for a SynRM as compared to that for an IPM machine, a SynRM should be able to use flux along the q-axis for back EMF-based sensorless control if the d-axis works for an IPM machine. This q-axis flux can be generated by injecting q-axis stator current.

If the above assumption holds, sensorless control using HFI method and back EMF method can be unified without running into the controversy regarding the stability of operation trajectory, as shown in Fig. 8.

A. Proposed Active Q Flux and Sensorless Control

In this section, "active q flux" concept is proposed to justify the above assumption. Sensorless control based on the active q flux concept is evaluated mathematically.

1) Active Q Flux Concept: The conventional active flux concept, as illustrated in (4), is considered as active d flux, where the final active flux vector λ^{af} aligns toward the d-axis. This is shown in Fig. 5. If the green dot-dash line ($L_q i_s$ vector) in Fig. 5 is extended further to intersect q-axis, as shown in Fig. 9(a), a new flux vector from origin to the q-axis intersection point (red line with arrow) is defined as "active q flux." Equation (11) shows its mathematical definition, where λ^{af-q} is the proposed active q flux, λ_d^{af-q} and λ_q^{af-q} are the active q fluxes on the dq
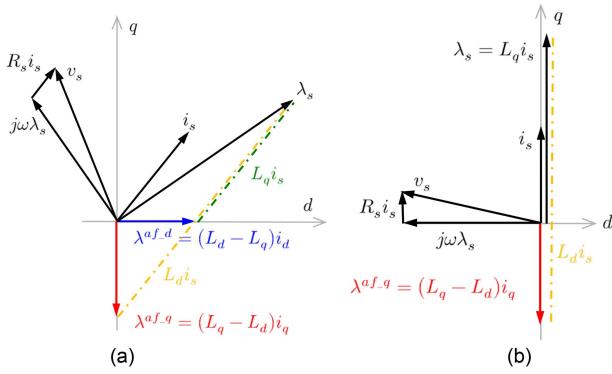
Fig. 9. Active *q* flux definition on *dq* current plane. (a) With both i_d and i_q current. (b) With only i_q current and zero i_d current.

Fig. 10. Rotor position estimation based on the proposed active *q* flux.

axes, respectively

$$
\begin{cases}
\lambda_d^{af\_q} = \lambda_d - L_d\, i_d = 0 \\
\lambda_q^{af\_q} = \lambda_q - L_d\, i_q = (L_q - L_d) \cdot i_q = \lambda^{af\_q}.
\end{cases} \tag{11}
$$

Fig. 9(a) shows that λ^{af_q} aligns itself toward the negative *q*-axis. The yellow dashed line that connects λ_s to λ^{af_q} is $L_d i_s$ vector. Fig. 9(b) shows that when only *q*-axis current is commanded, active *d* flux λ^{af_d} disappears, but active *q* flux λ^{af_q} still exists. In other words, active *q* flux is only a function of *q*-axis current. Now, the torque equation in (7) can be rewritten by substituting (11) into (6) as follows:

$$
T = -\frac{3}{2} p \lambda^{af\_q} i_d. \tag{12}
$$

2) Sensorless Control Using Active Q Flux: Based upon the proposed active *q* flux concept above, stator *dq* axes flux vector in (11) can be rewritten as follows:

$$
\begin{cases}
\lambda_d = L_d\, i_d \\
\lambda_q = L_d\, i_q + \lambda^{af\_q}
\end{cases} \tag{13}
$$

substituting (13) into (1) gives

$$
\begin{cases}
v_d = R_s\, i_d + \frac{d}{dt} L_d i_d - \omega L_d i_q - \omega \lambda^{af\_q} \\
v_q = R_s\, i_q + \frac{d}{dt} L_d i_q + \omega L_d i_d + \frac{d\lambda^{af\_q}}{dt}.
\end{cases} \tag{14}
$$

Considering λ^{af_q} as a constant at steady state and converting *dq* axes of (14) into $\alpha\beta$ axes yields

$$
\begin{cases}
v_\alpha = R_s\, i_\alpha + \frac{d}{dt} L_d i_\alpha - \omega \lambda^{af\_q} \cdot \sin\theta \\
v_\beta = R_s\, i_\beta + \frac{d}{dt} L_d i_\beta + \omega \lambda^{af\_q} \cdot \cos\theta.
\end{cases} \tag{15}
$$

Adopting the same rotor position estimation scheme, as presented in Section III-B, rotor position θ, using active *q* flux concept, can be calculated as

$$
\begin{aligned}
\theta &= \operatorname{atan} \frac{\lambda^{af\_q} \cdot \sin\theta}{\lambda^{af\_q} \cdot \cos\theta} + \frac{\pi}{2} \\
&= \operatorname{atan} \frac{\int (v_\beta - R_s i_\beta) - L_d i_\beta}{\int (v_\alpha - R_s i_\alpha) - L_d i_\alpha} + \frac{\pi}{2}.
\end{aligned} \tag{16}
$$

Equation (16) is translated into the control block diagrams, as shown in Fig. 10, where $\pi/2$ is added to the final angle estimation output that accounts for the orientation of active *q* flux along the negative *q*-axis, as shown in Fig. 9(a). Fig. 10 only shows the main framework regarding the implementation. Advanced sensorless algorithms, such as "sliding-mode observer" [31],

Fig. 11. Proposed minimum *q*-axis current trajectory as well as the conventional trajectory defined by a minimum *d*-axis current.

[32] or extended Kalman filter [33], [34], can enhance sensorless control performance, for example, allowing operation at lower operating speeds. However, this article focuses on the proposed active *q*-axis flux concept, which is independent of the sensorless algorithm utilized. For simplicity, the direct position calculations, as shown in Fig. 10, are analyzed in Section V.

B. SynRM Back EMF Sensorless Using Minimum Q-Axis Current Excitation

The proposed active *q* flux demonstrates that the rotor position can be estimated using the *q*-axis current-induced flux. Instead of maintaining a minimum *d*-axis current at the risk of destabilizing HFI sensorless control, a minimum *q*-axis current is retained at low torque condition, as shown in Fig. 11. Now, the current works on the *q*-axis limited excitation curve (green) at low torque condition and transits to MTPA curve (red) once large torque command is issued.

Comparing Fig. 11 with Fig. 8, this minimum *q*-axis current bypasses all HFI unstable region, as shown in Fig. 8, which serves as an improved trajectory for HFI and back EMF-integrated sensorless control.

C. Difference Between the Proposed Active Q Flux and Conventional Active D Flux

There are a few differences regarding back EMF-based sensorless control between using the proposed active *q* flux and conventional active *d* flux.
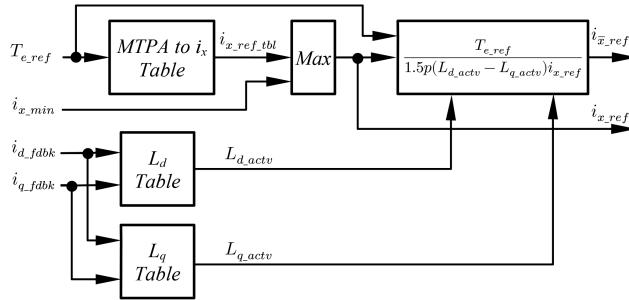
Fig. 12. Current reference generation for a given torque reference. For conventional active *d* flux, $i_x = i_d$ and $i_{\bar{x}} = i_q$. For the proposed active *q* flux, $i_x = i_q$ and $i_{\bar{x}} = i_d$.
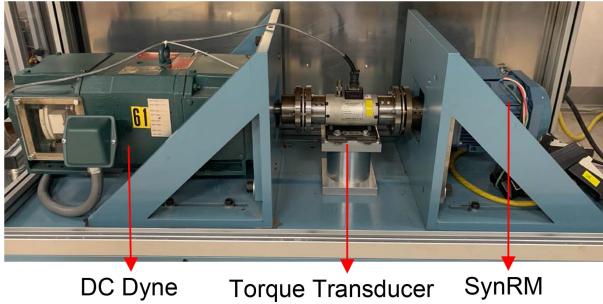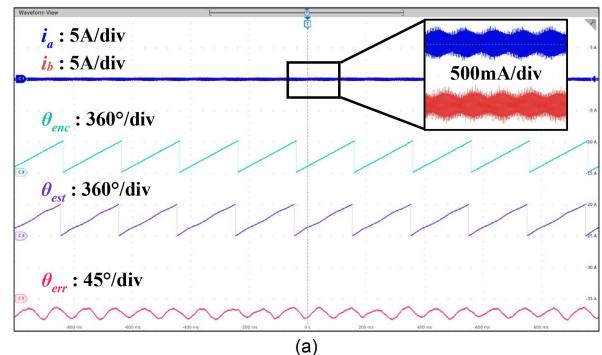
Fig. 13. Experimental dyne setup.

1) In Fig. 9(a), active *q* flux lags active *d* flux by 90 electrical degrees, which indicate 90° estimated angle difference. This is compensated in (16) and Fig. 10.

2) Since *q*-axis inductance L_q is smaller than *d*-axis inductance L_d, for the same amount of current, the *q*-axis-induced flux will be lower than the *d*-axis. Therefore, the transition speed from HFI to back EMF may need to be adjusted higher for *q*-axis injection, so back EMF sensorless method will not fail due to insufficient back EMF voltage.

3) Calculation of *d* and *q* current references requires a slight modification. In the conventional approach, i_d is determined using an MTPA lookup table, and i_q is calculated using the torque equation. In the proposed approach, these methods are flipped, so i_q is from a lookup table, and i_d is calculated. This is shown in Fig. 12.
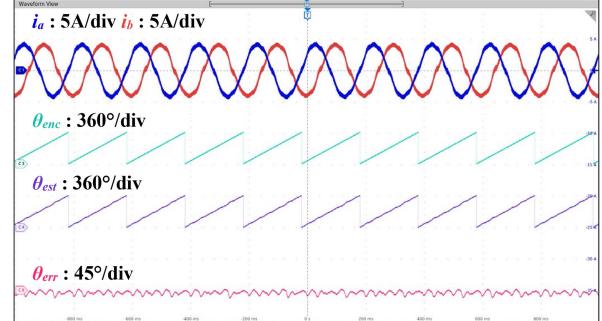
V. EXPERIMENTAL RESULTS

Experimental data were collected to demonstrate the proposed active *q* flux concept and its enhancement toward the sensorless control. The specification of the SynRM motor under test is shown in Table I and the overall system control block diagram and sensorless control diagram are shown in Figs. 4 and 10, respectively. Fig. 13 shows the dyne setup used for data collection. For all tests, speed regulation is achieved using the dyne.
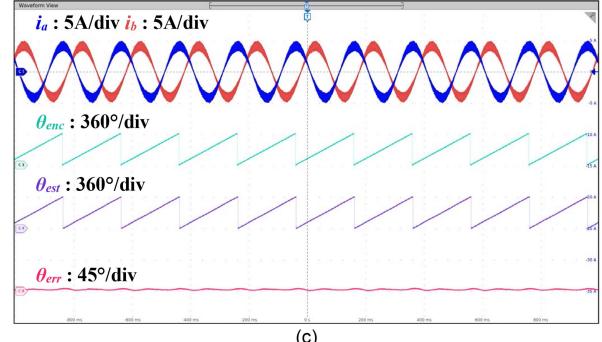
Five experiments are conducted, where experiments A and B compare sensorless angle estimation using HFI method under no-load (zero torque) and light-load (25% torque) conditions, and experiments C and D look at back EMF-based sensorless angle estimation using active *d* flux and the proposed active *q*

Fig. 14. HFI angle detection with zero torque output. (a). Original with 0 i_d and 0 i_q. (b) Active *d* flux with 40% i_d current and zero i_q current. (c) Active *q* flux with 40% i_q and zero i_d current. Horizontal axis scale: **200 ms/div.**

flux under no-load and full-load conditions, and experiment E evaluates the waveforms of the transition period between HFI and back EMF sensorless methods. The annotations for different curves in Figs. 15–19 are listed as follows:

i_a	phase *a* current.
i_b	phase *b* current.
θ_{enc}	encoder angle feedback.
$\theta_{\text{est\_d}}$	estimated angle feedback using active *d* flux.
$\theta_{\text{est\_q}}$	estimated angle feedback using active *q* flux.
θ_{est}	final estimated angle feedback.
θ_{err}	angle error $\theta_{\text{enc}} - \theta_{\text{est}}$.

The exact capability of this sensorless SynRM motor drive in terms of maximum torque/speed range is not explored since it is not the intention of this article.

A. HFI With Zero Torque Output (5 Hz, 150 r/min)

The constant torque curve in Fig. 4 shows SynRM outputs zero torque when the current operation point is either on the
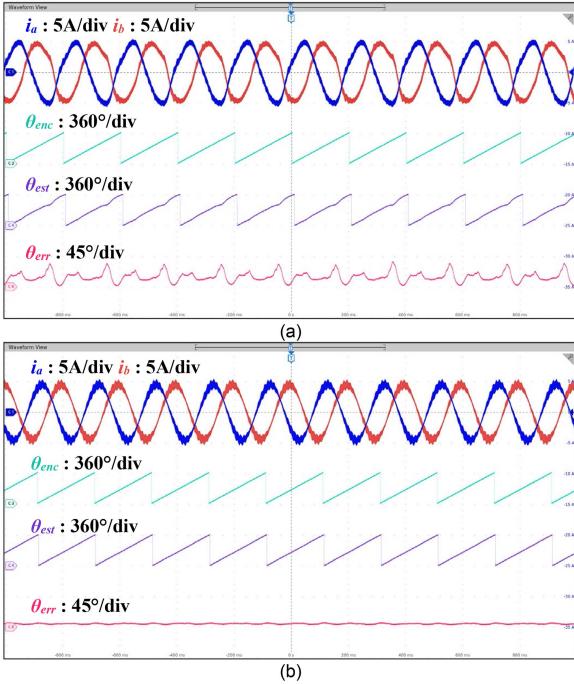
Fig. 15. HFI angle detection with 25% rated load. (a) $i_d = 4$ A and $i_q = 2.23$ A. (b) $i_d = 1.76$ A and $i_q = 4.0$ A. Horizontal axis scale: **200 ms/div.**
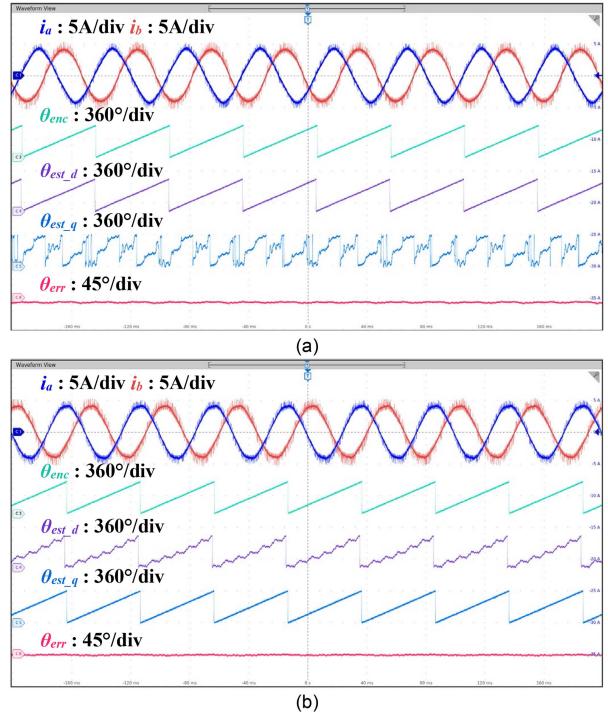
Fig. 16. Back EMF-based angle detection at no-load condition. (a) Active d flux. (b) Active q flux. Horizontal axis scale: **40 ms/div**.

Fig. 17. Back EMF-based angle detection with active q flux concept at rated torque condition. Horizontal axis scale: **100 ms/div**.

d-axis or q-axis. In this experiment, three operational points are selected to compare HFI sensorless angle output.

Fig. 14(a) compares HFI estimated angle versus encoder feedback angle when drive operates at the origin of current vector plane, as explained in Section III-E and Fig. 8. The estimated angle θ_{est} shows low-order harmonics, which is confirmed by θ_{err} in Fig. 14(a). Meanwhile, a constant angle error (more than 20°) is observed in θ_{err}.

Fig. 14(b) shows the same waveforms after injecting 40% i_d current and 0 i_q current. The ripple on the estimated angle θ_{est} becomes higher in frequency but smaller in peak-to-peak amplitude. Furthermore, the estimated angle error θ_{err} shows less average value.

On the other hand, Fig. 14(c) shows the waveforms with 0 i_d and 40% i_q. The estimated angle θ_{est} shows almost perfect saw-tooth triangle without noticeable oscillation. The estimated angle error θ_{err} is close to zero with slight ripple.

The improvements can also be identified from comparing the measured phase A and phase B currents in both Fig. 14(b) and (c). In Fig. 14(b), HFI injected harmonic currents show even current ripple at different rotor position, which suggests a small saliency ratio between the d and q axes. This agrees with the analysis in Section I-D and E, where the injected d-axis current decreases saliency ratio. On the other hand, HFI current ripple in Fig. 14(c) shows position dependency, which is an indicator of saliency. The excessive ripple on the estimated angle, as shown in Fig. 14(b), acts as a disturbance to the system, which causes output torque ripple.

The data collected in this section demonstrate that when zero torque output is desired, commanding a minimum q-axis current can improve HFI position estimation compared to the cases
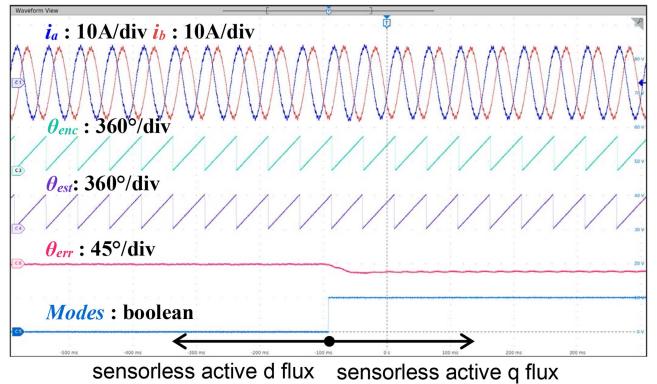
without a minimum current command, or where the minimum current is commanded on the d-axis.

B. HFI With Low Torque (25% Rated) Output (5 Hz, 150 r/min)

To further demonstrate the improvement toward HFI sensorless control using q-axis current injection, a small torque (25% rated) is applied. Fig. 15 shows two operational cases. The first operational point locates on minimum d-axis current excitation curve with around 40% i_d and 22% i_q ($i_d = 4$ A and $i_q = 2.23$ A) selected, which outputs 25% of the rated torque. The result waveforms are shown in Fig. 15(a), where phase currents are distorted and estimated position θ_{est} oscillates.

By contrast, Fig. 15(b) shows the case with around 40% i_q and 18% i_d ($i_d = 1.76$ A and $i_q = 4.0$ A), which operates on
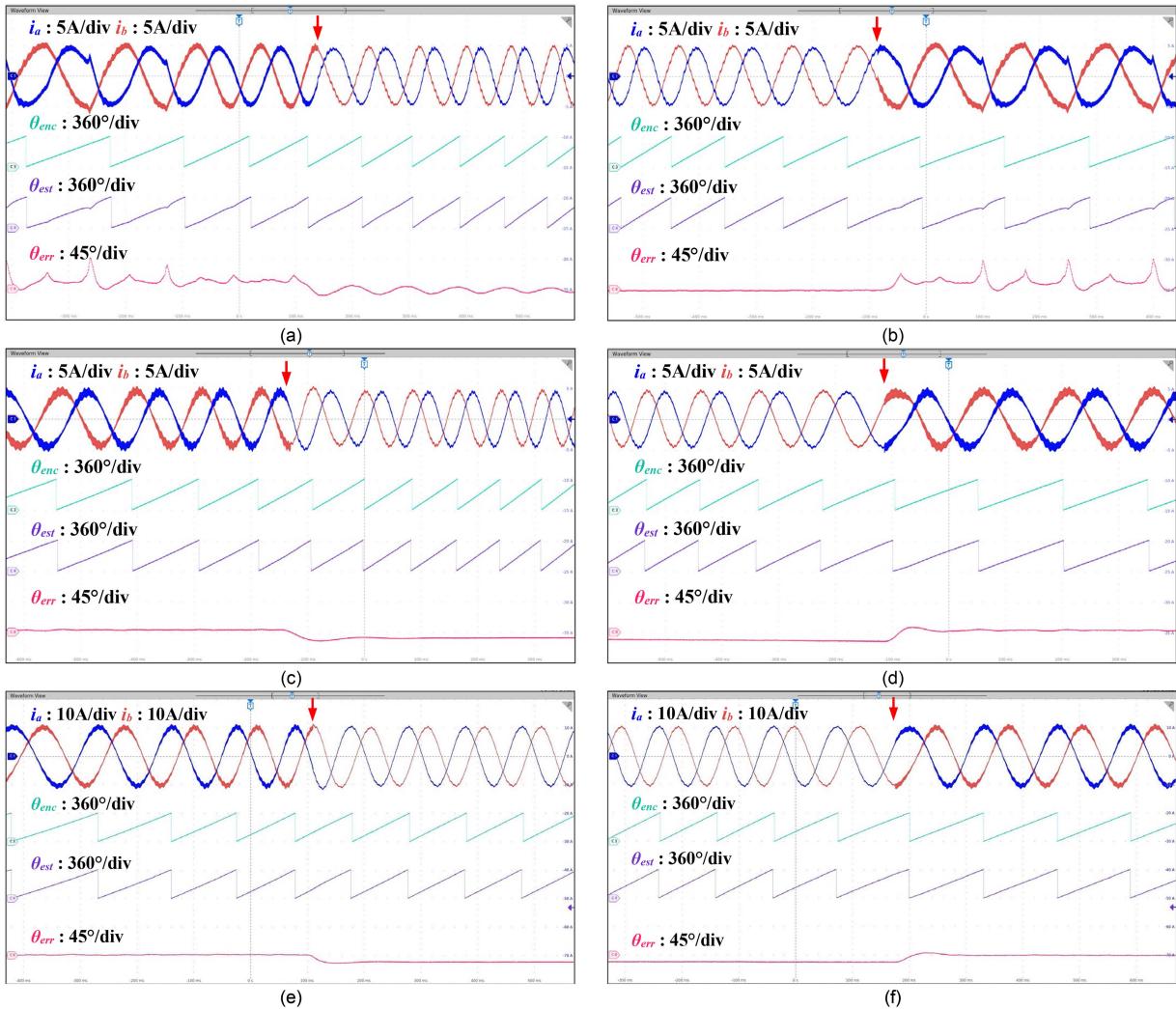
Fig. 18. Sensorless methods transition between HFI and back EMF. (a) HFI to back EMF with active *d* flux at 25% load condition. (b) Back EMF to HFI with active *d* flux at 25% load condition. (c) HFI to back EMF with active *q* flux at 25% load condition. (d) Back EMF to HFI with active *q* flux at 25% load condition. (e) HFI to back EMF with active *q* flux at 100% load condition. (f) Back EMF to HFI with active *q* flux at 100% load condition. The red arrow on each figure denotes the transition moment. Horizontal axis scale: **100 ms/div**.

minimum *q*-axis current excitation curve. It also delivers 25% rated torque according to the constant torque curve, as shown in Fig. 4. The phase current harmonics are eliminated, and the estimated angle oscillations are significantly attenuated.

The data in this section demonstrate that when low, nonzero torque output is desired, commanding a minimum *q*-axis current can improve HFI position estimation compared to the case where a minimum current is commanded on the *d*-axis.

C. Back EMF Method Without Load (20 Hz, 600 r/min)

Experiments A and B validate the proposed *q*-axis current injection toward the enhancement of sensorless operation using HFI at low speed. Experiments C and D try to demonstrate that the back EMF-based sensorless control is still functioning after adopting the proposed active *q* flux concept as compared to the conventional active *d* flux method.

This section first tests the operation under no load condition. Fig. 16(a) shows the waveforms of sensorless control with

conventional active *d* flux (40% i_d, 0 i_q). The estimated angle θ_{est_d} using active *d* flux method, as explained in Section I-B, tracks encoder angle θ_{enc} tightly. This is confirmed by θ_{err}, which is the difference between θ_{est_d} and θ_{enc}. However, estimated angle θ_{est_q} using active *q* flux described in Section I-A2 does not show a meaningful result because active *q* flux does not exist when only *d*-axis current is injected.

On the other hand, Fig. 16(b) presents the experimental result with the proposed active *q* flux (0 i_d, 40% i_q). This time, the estimated angle θ_{est_q} using active *q* flux shows the promising result with smooth saw-tooth triangle. This is manifested in θ_{err} accordingly. Estimated angle θ_{est_d} using active *d* flux shows considerable ripple because no *d*-axis current is commanded, albeit the angle of θ_{est_d} is still following the encoder feedback θ_{enc} in average. This could attribute to the fact that a part of the *q*-axis flux runs through the *d*-axis lamination when large *q*-axis current already saturates *q*-axis lamination.

The data in this section demonstrate that when zero torque output is desired, sensorless operation by commanding a minimum
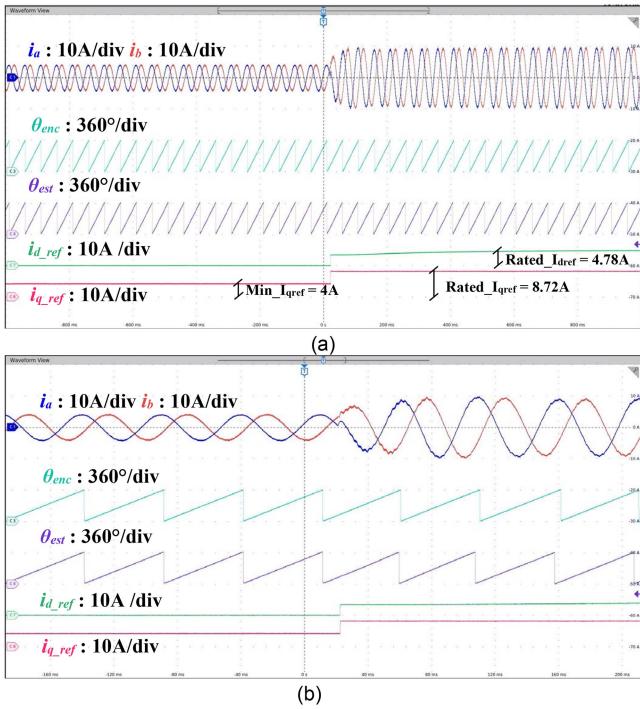
Fig. 19. 0%–100% step load test with the proposed active q flux concept. (b) is the zoomed view of (a) at the step load moment. (a) (**200 ms/div**). (b) (**40 ms/div**).

q-axis current produces a result comparable to the sensorless operation by commanding a minimum d-axis current.

D. Back EMF With Rated Load (20 Hz, 600 r/min)

Operating with rated torque on MTPA curve is essential to prove the effectiveness of the proposed sensorless control with active q concept. Fig. 17 shows the sensorless control with rated torque output on MTPA curve ($i_d = 4.78$ A and $i_q = 8.72$ A). Both active d flux concept and active q flux concept are exercised.

Under rated condition, both d-axis and q-axis currents are commanded to produce rated torque. Consequently, adequate d-axis and q-axis fluxes are excited for sensorless control using either active d flux or active q flux. Fig. 17 shows a consistent angle detection depicted in θ_{est} before and after algorithm switch. In addition, the switch from sensorless control with active d flux in left half of the figure to sensorless control with active q flux in right half is almost bumpless. However, the sensorless angle estimation accuracy varies with different methods, as shown in θ_{err}. Although $|\theta_{err}|$ increases when using q-axis flux compared with d-axis flux, the torque transducer showed a similar average torque output in both cases: 19.3 N·m for d-axis flux and 19.1 N·m for q-axis flux. These torque meter results show that the effect is not significant, but the cause of increased $|\theta_{err}|$ requires further investigation, as the resulting decrease in torque per amp is certainly undesirable.

The data in this section demonstrate that when rated torque output is desired, sensorless operation under the proposed active q flux concept is stable. It produces results that are comparable to the conventional active d flux approach.

E. Transition Between HFI and Back EMF

The proposed active q flux enables operating on the same current vector point for both HFI and back EMF sensorless methods. The transition waveforms with the conventional active d flux and new active q flux are both captured in Fig. 18. The transition speed from HFI method to back EMF method is set at 300 r/min, and reverse transition speed is set at 225 r/min. The transition speed difference above creates a hysteresis period that can prevent jittering between HFI and back EMF methods. These transition thresholds are determined empirically. The acceleration and deceleration rates are set at 150 r/min/s.

Fig. 18(a)–(d) compares the transition waveforms between the conventional active d flux and the proposed active q flux at 25% torque command. With the conventional active d flux in Fig. 18(a), the estimated angle oscillates soon after the transition and the oscillation damps out gradually. However, by adopting the active q flux, the angle in Fig. 18(c) is smooth and stable before and after the transition.

Fig. 18(e) and (f) demonstrates the smoothness of the transition between HFI and back EMF and vise-versa when the motor operates at 100% load condition.

F. 0%–100% Step Load Test (20 Hz, 600 r/min)

Finally, a 0%–100% step load test is conducted to further validate the proposed active q flux concept. Fig. 19 demonstrates the stable torque step response. Before the torque step, the motor runs at the minimum q-axis excitation current (0 i_d, 40% i_q). An MTPA lookup table defines i_{q_ref} after 100% torque step is commanded. Torque equation (3) is used to calculate i_{d_ref}. Note that the fluxes in (3) are defined using inductance maps (2), which utilize measured currents. Thus, i_{d_ref} increases from 3.4 to 4.78 A, as its calculated value is adjusted as L_d and L_q are updated with measured currents.
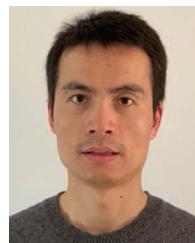
VI. CONCLUSION

In this article, a position sensorless approach utilizing a minimum q-axis current was proposed for high- and low-speed operation of SynRM. In the low-speed range, using a minimum q-axis resulted in an operating trajectory that can improve the estimated rotor position by avoiding regions of instability associated with HFI algorithms. Furthermore, sensorless operation at high-speed using active q flux concept was demonstrated. Using the same current trajectory across the entire speed range simplified transitioning between the high- and low-speed methods. The proposed concept was validated by the experimental results.

REFERENCES

[1] A. Boglietti, A. Cavagnino, M. Pastorelli, and A. Vagati, "Experimental comparison of induction and synchronous reluctance motors performance," in *Proc. 4th IAS Annu. Meeting Conf. Rec. Ind. Appl. Conf.*, Hong Kong, China, 2005, pp. 474–479.

[2] N. Bianchi, "Synchronous reluctance and interior permanent magnet motors," in *Proc. IEEE Workshop Elect. Mach. Des., Control Diagnosis*, Paris, France, Mar. 2013, pp. 75–84.

[3] A. Yousefi-Talouki, P. Pescetto, G. Pellegrino, and I. Boldea, "Combined active flux and high-frequency injection methods for sensorless direct-flux vector control of synchronous reluctance machines," *IEEE Trans. Power Electron.*, vol. 33, no. 3, pp. 2447–2457, Mar. 2018.

[4] A. Yousefi-Talouki, P. Pescetto, and G. Pellegrino, "Sensorless direct flux vector control of synchronous reluctance motors including standstill, MTPA, and flux weakening," *IEEE Trans. Ind. Appl.*, vol. 53, no. 4, pp. 3598–3608, Jul./Aug. 2017.

[5] F. J. W. Barnard, W. T. Villet, and M. J. Kamper, "Hybrid active-flux and arbitrary injection position sensorless control of reluctance synchronous machines," *IEEE Trans. Ind. Appl.*, vol. 51, no. 5, pp. 3899–3906, Sep./Oct. 2015.

[6] T. Tuovinen and M. Hinkkanen, "Adaptive full-order observer with high-frequency signal injection for synchronous reluctance motor drives," *IEEE J. Emerg. Sel. Topics Power Electron.*, vol. 2, no. 2, pp. 181–189, Jun. 2014.

[7] S.-C. Agarlita, I. Boldea, and F. Blaabjerg, "High-frequency-injection-assisted "active-flux"-based sensorless vector control of reluctance synchronous motors, with experiments from zero speed," *IEEE Trans. Ind. Appl.*, vol. 48, no. 6, pp. 1931–1939, Nov./Dec. 2012.

[8] E. Capecchi, P. Guglielmi, M. Pastorelli, and A. Vagati, "Position-sensorless control of the transverse-laminated synchronous reluctance motor," *IEEE Trans. Ind. Appl.*, vol. 37, no. 6, pp. 1768–1776, Nov./Dec. 2001.

[9] S.-J. Kang, J.-M. Kim, and S.-K. Sul, "Position sensorless control of synchronous reluctance motor using high frequency current injection," *IEEE Trans. Energy Convers.*, vol. 14, no. 4, pp. 1271–1275, Dec. 1999.

[10] P. Pescetto, A. Yousefi-Talouki, and G. Pellegrino, "Novel sensorless control algorithm for SyR machines based on low speed active flux," in *Proc. IEEE 10th Int. Symp. Sensorless Control Elect. Drives*, 2019, pp. 1–6.

[11] A. Varatharajan and G. Pellegrino, "Sensorless control of synchronous reluctance motor drives: Improved modeling and analysis beyond active flux," in *Proc. IEEE Int. Elect. Mach. Drives Conf .*, 2019, pp. 419–426.

[12] A. Varatharajan, G. Pellegrino, and E. Armando, "Sensorless synchronous reluctance motor drives: Auxiliary flux-based position observer," *IEEE J. Emerg. Sel. Topics Power Electron.*, vol. 9, no. 4, pp. 4330–4339, Aug. 2021.

[13] A. Farhan, M. Abdelrahem, A. Saleh, A. Shaltout, and R. Kennel, "High-performance position sensorless control of reluctance synchronous motor using high-frequency injection," in *Proc. IEEE 13th Int. Conf. Power Electron. Drive Syst.*, 2019, pp. 1–6.

[14] A. Varatharajan, G. Pellegrino, and E. Armando, "Signal-injection sensorless control of synchronous reluctance machines for overload operation," *IEEE Trans. Power Electron.*, vol. 37, no. 5, pp. 5874–5883, May 2022.

[15] I. Boldea, M. C. Paicu, and G.-D. Andreescu, "Active flux concept for motion-sensorless unified AC drives," *IEEE Trans. Power Electron.*, vol. 23, no. 5, pp. 2612–2618, Sep. 2008.

[16] W. T. Villet, M. J. Kamper, P. Landsmann, and R. Kennel, "Hybrid position sensorless vector control of a reluctance synchronous machine through the entire speed range," in *Proc. 15th Int. Power Electron. Motion Control Conf.*, Novi Sad, Serbia, 2012, pp. 1–7.

[17] M. Hinkkanen, P. Pescetto, E. Mölsä, S. E. Saarakkala, G. Pellegrino, and R. Bojoi, "Sensorless self-commissioning of synchronous reluctance motors at standstill without rotor locking," *IEEE Trans. Ind. Appl.*, vol. 53, no. 3, pp. 2120–2129, May/Jun. 2017.

[18] N. Bedetti, S. Calligaro, and R. Petrella, "Stand-still self-identification of flux characteristics for synchronous reluctance machines using novel saturation approximating function and multiple linear regression," *IEEE Trans. Ind. Appl.*, vol. 52, no. 4, pp. 3083–3092, Jul./Aug. 2016.

[19] A. Vagati, M. Pastorelli, and G. Franceschini, "High-performance control of synchronous reluctance motors," *IEEE Trans. Ind. Appl.*, vol. 33, no. 4, pp. 983–991, Jul./Aug. 1997.

[20] F. Tinazzi, S. Bolognani, S. Calligaro, P. Kumar, R. Petrella, and M. Zigliotto, "Classification and review of MTPA algorithms for synchronous reluctance and interior permanent magnet motor drives," in *Proc. 21st Eur. Conf. Power Electron. Appl.*, 2019, pp. 1–10.

[21] P. Niazi, H. A. Toliyat, and A. Goodarzi, "Robust maximum torque per ampere (MTPA) control of PM-assisted SynRM for traction applications," *IEEE Trans. Veh. Technol.*, vol. 56, no. 4, pp. 1538–1545, Jul. 2007.

[22] P. L. Jansen and R. D. Lorenz, "Transducerless position and velocity estimation in induction and salient AC machines," *IEEE Trans. Ind. Appl.*, vol. 31, no. 2, pp. 240–247, Mar./Apr. 1995.

[23] M. Schroedl, "Sensorless control of AC machines at low speed and standstill based on the "INFORM" method," in *Proc. Conf. Rec. IEEE Ind. Appl. Conf. 31st IAS Annu. Meeting*, 1996, pp. 270–277.

[24] J. Cilia, G. M. Asher, K. J. Bradley, and M. Sumner, "Sensorless position detection for vector-controlled induction motor drives using an asymmetric outer-section cage," *IEEE Trans. Ind. Appl.*, vol. 33, no. 5, pp. 1162–1169, Sep./Oct. 1997.

[25] J.-H. Jang, S.-K. Sul, J.-I. Ha, K. Ide, and M. Sawamura, "Sensorless drive of surface-mounted permanent-magnet motor by high-frequency signal injection based on magnetic saliency," *IEEE Trans. Ind. Appl.*, vol. 39, no. 4, pp. 1031–1039, Jul./Aug. 2003.

[26] J.-I. Ha and S.-K. Sul, "Sensorless field orientation control of an induction machine by high frequency signal injection," in *Proc. Conf. Rec. IEEE Ind. Appl. Conf. 32nd IAS Annu. Meeting*, New Orleans, LA, USA, 1997, vol. 1, pp. 426–432.

[27] Y.-D. Yoon, S.-K. Sul, S. Morimoto, and K. Ide, "High-bandwidth sensorless algorithm for AC machines based on square-wave-type voltage injection," *IEEE Trans. Ind. Appl.*, vol. 47, no. 3, pp. 1361–1370, May/Jun. 2011.

[28] P. Guglielmi, M. Pastorelli, and A. Vagati, "Impact of cross-saturation in sensorless control of transverse-laminated synchronous reluctance motors," *IEEE Trans. Ind. Electron.*, vol. 53, no. 2, pp. 429–439, Apr. 2006.

[29] D. Xiao et al., "Universal full-speed sensorless control scheme for interior permanent magnet synchronous motors," *IEEE Trans. Power Electron.*, vol. 36, no. 4, pp. 4723–4737, Apr. 2021.

[30] A. Vagati, "The synchronous reluctance solution: A new alternative in AC drives," in *Proc. 20th Annu. Conf. IEEE Ind. Electron.*, Bologna, Italy, 1994, vol. 1, pp. 1–13.

[31] S. Chi, Z. Zhang, and L. Xu, "Sliding-mode sensorless control of direct-drive PM synchronous motors for washing machine applications," *IEEE Trans. Ind. Appl.*, vol. 45, no. 2, pp. 582–590, Mar./Apr. 2009.

[32] G. Wang, R. Yang, and D. Xu, "DSP-based control of sensorless IPMSM drives for wide-speed-range operation," *IEEE Trans. Ind. Electron.*, vol. 60, no. 2, pp. 720–727, Feb. 2013.

[33] S. Bolognani, L. Tubiana, and M. Zigliotto, "EKF-based sensorless IPM synchronous motor drive for flux-weakening applications," *IEEE Trans. Ind. Appl.*, vol. 39, no. 3, pp. 768–775, May/Jun. 2003.

[34] S. Bolognani, L. Tubiana, and M. Zigliotto, "Extended Kalman filter tuning in sensorless PMSM drives," *IEEE Trans. Ind. Appl.*, vol. 39, no. 6, pp. 1741–1747, Nov./Dec. 2003.

[35] N. Bianchi, S. Bolognani, D. Bon, and M. D. Pré, "Rotor flux-barrier design for torque ripple reduction in synchronous reluctance and PM-assisted synchronous reluctance motors," *IEEE Trans. Ind. Appl.*, vol. 45, no. 3, pp. 921–928, May/Jun. 2009.

Zhendong Zhang (Member, IEEE) received the B.S. degree in electrical engineering from Southeast University, Nanjing, China, the Graduate degree from Tsinghua University, Beijing, China, and the Ph.D. degree from the Department of Electrical Engineering, The Ohio State University, Columbus, OH, USA, in 2006, 2008, and 2013, respectively.

He was an intern with United Technology Research Center in 2013. He is currently with Standard Drives Division, Rockwell Automation, Mequon, WI, USA. His primary interests include the application of power electronics to variable-speed drive.

Jacob Lamb (Member, IEEE) received the B.S. degree in mathematics and the B.S.E. degree in electrical engineering from Northern Arizona University, Flagstaff, AZ, USA, both in 2013, and the Ph.D. degree in electrical engineering from Kansas State University, Manhattan, KS, USA, in 2017.

He is currently a Senior Electrical Engineer with Milwaukee Tool, Brookfield, WI, USA. His research interests include power electronics and switching algorithms for fault tolerance in reconfigurable converters.